Towards a Wireless Force Sensor Based on Wave Backscattering for Medical Applications
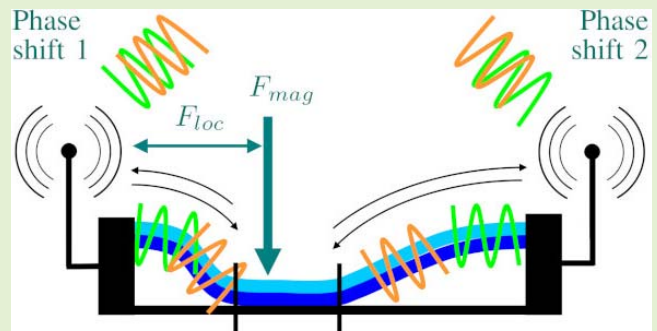
Cédric Girerd, Qiming Zhang, Agrim Gupta, Manideep Dunna, Dinesh Bharadia, *Member, IEEE*, and Tania. K. Morimoto, *Member, IEEE*

Abstract—In medical applications, sensing forces along surgical tools is of high importance in order to avoid collateral damage of tissue and surrounding structures. However, the space available in their central lumen limits the routing of wired sensors that are widely available today, and thus their integration into such tools. In this paper, we present a new wireless force sensor based on wave backscattering that reflects electromagnetic waves with phase changes that are directly related to the applied force magnitude and location. The proposed sensor can sense force magnitudes with an average error of 0.01 N and a standard deviation of 0.49 N, and their application location with an average error of -0.33 mm and a standard deviation of 0.82 mm. The sensor also has the potential to be translated to applications beyond medical instruments, including applications involving a large number of sensors and situations where wire routing is challenging due to the environment in which they are used.

Index Terms— Force sensors, electromechanical sensors, robot sensing systems, wireless sensors.

I. INTRODUCTION

AS robots and humans interact more closely and as robots are required to perform more complicated and dexterous tasks, force information becomes increasingly important. Sensing the forces applied by the robot to the environment allows them to detect contact with objects, as well as grasp and manipulate delicate objects [1], leading to overall safer and more dexterous operations. Several types of sensors, each based on different physical principals [1]–[4], have been developed in recent years to address these needs. The applications of these sensors are diverse, with use in industrial automation, the military, agriculture, the food industry, and medical domains.

Integration of force sensors in medical devices and surgical instruments, in particular, is of high importance [2]–[4]. Despite its many benefits, teleoperated robot-assisted

minimally invasive surgery is limited by the inability of current instruments to sense forces applied during surgery [5]. This phenomena leads to surgeons relying only on visual feedback to perform surgical tasks, which gives limited, indirect information. The ability to sense forces at the tip of the robotic instruments is important in order to limit the applied forces and prevent damaging the underlying anatomical structures during milling or cutting tasks. In addition, sensing forces along the entire length of these robotic instruments is important in order to avoid damaging the surrounding environment and to estimate their deflection during operation. Integrated sensing along the entire length is particularly important for continuum robots, which are small (diameters as small as 1 millimeter [6]), continuously bending, flexible structures that are especially well-suited for minimally-invasive surgery. Current approaches for sensing forces along the length of these robots involve the use of optical fibers [7]–[9], including light intensity modulation [10]–[13], Fabry–Perot interferometers, and Fiber Bragg Grating (FBG) methods [14], [15]. Despite having many advantages, these sensors are either costly, or suffer from undesired drifts and light intensity loss that can lead to measurement errors [9]. A recent approach proposes the use of force sensitive resistors [16]. However, a higher number of these sensors are required to obtain more complete measurements of the entire loading state of a robot, and the central lumen of these robots is reserved as passageway for surgical instruments. These constraints therefore lead to a challenge with respect to the placement and wire routing of sensors inside these small structures.

A. Force Sensor Technologies

Force sensors to date have used a variety of different physical principals, and generally take the form of transducers, by converting the mechanical energy of a physical contact to an electrical signal [3]. The main types of sensors commercially available today include force sensitive resistors [16], piezoelectric [17], capacitive, inductive, optical [8], [13], ultrasonic, magnetic, electromagnetic (EM) tracking systems and electrical impedance tomography sensors. Some sensors also implement a combination of physical principals to overcome their individual limitations [2].

While these sensors may vary in terms of both working mechanism and in terms of performance, they all provide an input that is not suitable for direct wireless communication, and therefore require additional electronics to encode their outputs in a suitable format [18]. This requirement typically leads to an increase in the size of these sensors, which is not suitable for integration with small robotic instruments or with use in constrained environments. In addition, these sensors need to be powered electrically or need a light source, leading to the need for physical connections between the sensor and an external base. The requirement of maintaining a physical connection poses a wire routing issue when the sensors are mounted on remote structures, when a large number of sensors are used, or when the sensors are located in confined spaces.

A few examples of wireless force sensors are proposed in the literature, including LC resonant circuits [19] and strain sensors based on electromagnetically soft materials [20]. However, LC resonant circuits require a close interrogation distance between the sensor and the readout circuits – on the order of magnitude of a centimeter – and are accompanied with issues due to misalignment, noise from the environment, and cross-talking among elements [21]. Similarly, the wireless force sensors based on electromagnetically soft materials require multiple large coils in close proximity to the sensor [20], which is not practical for most applications in confined spaces.

B. Integrating Sensing With Wave Backscattering

Wave backscaterring systems differ from conventional communication systems. Rather than actively generating a wireless signal from a source of energy to communicate, they simply reflect ambient signals sent by transmitting antennas. The properties of the signal traveling through the backscattering system, including phase [22], amplitude [23], and frequency [24], encode the information to be communicated. The reflected signal is then measured by receiving antennas.

To date, a few groups have used wave backscattering to sense binary contact information (i.e. contact or no contact) [22]–[29]. IDSense [23] used a combination of amplitude and phase changes to detect contact information with a backscaterring RFID tag, and PaperId [29] showed a simple manufacturing method to print these RFID tags using an inkjet printer and paper. RIO [22] showed how to sense contact on multiple tags by using phase changes due to mutual coupling of the tags. LiveTag [24] further extended this contact sensing to be performed via WiFi access points instead of dedicated RFID readers as used by previous work. Although these backscatter-based sensors are very simple in their structure and easy to manufacture, they are limited to binary measurements of contact/no-contact, and analog force sensing has yet to be proposed in this context.

There has been one recent example of a type of backscatter-based sensor, known as a SAW (Surface Acoustic Waves) based strain sensor, that aims to sense analog forces. These passive strain sensors [30]–[33] encode the strain information in terms of resonance frequency shifts in the backscattered signal. The strain readings are then inferred at the receiver by estimating the amplitudes at multiple frequencies to detect the frequency shift. However, most of the works show evaluations in a controlled, anechoic environment, and the technology has not been found to be robust to static multipath [31].

C. Contributions

In this paper, we present a new wireless force sensor capable of detecting both the magnitude and location of an applied force. It differs from the existing sensor technologies in its integrated wireless capability that does not require the use of additional electronics for conversion of force information into a suitable format for wireless communication. It is based on the wave backscattering principal, and the developed prototype consists of three main components: (i) a mechanical beam that when pressed into a rigid base, results in a contact with edge locations that depend on the force magnitude and its application location, (ii) a signal and ground trace that cover the mechanical beam and rigid base, respectively, and convert the mechanical contact into an electrical contact, and (iii) antennas that are connected to these traces. The antennas receive electromagnetic waves that propagate inside the signal trace, get reflected at the shorting location between the signal and ground traces, and are re-emitted passively by the sensor, thus following a backscattering principal, with phase shifts that depend on both the magnitude and location of the force applied.

The paper is organized as follows: Section II details the concept of the sensor. Design rules are then presented in Sections III and IV for the mechanical transducer and the electrical trace, respectively. The wireless sensing algorithm is then presented in Section V. An implementation of the sensor based on design specifications is presented in Section VI, and assessment of mechanical, wired, and wireless performance of the sensor are presented in Section VII. Conclusions and perspectives are finally presented in Section VIII.

II. PROPOSED CONCEPT

In this section, the sensor architecture and working principle are presented.

A. Sensor Concept

The proposed sensor is based on the principle of electromagnetic wave backscattering. It consists of a wireless reader that emits an electromagnetic wave. When this wave reaches the proposed sensor, it travels along an electrical trace from both ends of the sensor, is reflected back at shorting locations with a ground trace, and thus travels back along the direction
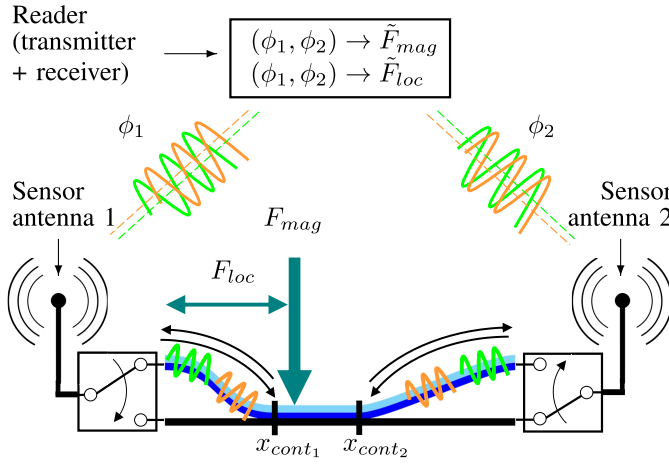
Fig. 1. Illustration of the sensor, which is composed of a bilayer beam (in light and dark blue) and a rigid base (in black). The edges of the contact length between these two components are denoted x_{cont_1} and x_{cont_2}. These components are also covered by contact traces that carry electromagnetic waves, shown in green and orange, through two antennas located at both ends of the sensor. These phases, denoted ϕ_1 and ϕ_2 after reflection, are measured by the reader and used to determine the applied force magnitude (F_{mag}) and location (F_{loc}).

from which it came. This reflected wave is then detected by the wireless reader, as illustrated in Fig. 1. We propose a sensor that induces changes in the total distance traveled by two reflected electromagnetic waves when a force is applied. We propose to measure the changes in the distances traveled by measuring the associated phase changes of the reflected waves. Knowing the relationship between the force magnitude, the location of this applied force, and the phase changes measured, the device becomes a force sensor, able to detect both the magnitude and application location of a force.

B. Sensor Overview

The sensor is composed of three main components. The first component is a mechanical transducer, able to deform uniquely upon application of a force magnitude and application location. For this component, we propose to used a fixed-ended bilayer beam, with the layers represented in light and dark blue in Fig. 1. Upon application of a force, this beam is pressed into contact with a rigid base, represented in black in Fig. 1. The edges of the corresponding contact length are denoted x_{cont_1} and x_{cont_2} (see Fig. 1). The top layer of the bilayer beam is stiffer than the bottom layer, such that the applied force is distributed onto the softer bottom layer, leading to an increasing contact length with the rigid base as the applied force is increased. The location of the contact edges between the bilayer beam and the rigid base informs us of the force magnitude and its application location.

The second component of the sensor consists of two electrical traces that cover the bottom side of the bilayer beam and the top side of the rigid base. The trace covering the bilayer beam is the signal trace, while the one covering the rigid base is the ground trace. The signal trace converts the mechanical contact locations x_{cont_1} and x_{cont_2} between the bilayer beam and the rigid base into electrical shorting locations when it touches the ground trace. This phenomena leads to the reflection of the emitted electromagnetic waves at the shorting locations, as visible in Fig. 1.

The last component is the wireless hardware and associated algorithm that senses the phases ϕ_1 and ϕ_2 of the signals that are reflected at the shorting locations on the signal trace (see Fig. 1). In order for the reader to distinguish the signal reflected by the sensor and the one initially sent to it, RF switches are used on both ends of the sensor to module the reflected signal before it is re-emitted by the sensor, as visible in Fig 1. These three main components are presented in the following sections, and the main associated variables used are visible in Table I.

III. MECHANICAL TRANSDUCER DESIGN

In this section, we present a design method for the mechanical transducer of the sensor. The method is split into two parts based on the stages of deflection of the bilayer beam. The first part involves multilayer beam mechanics to describe the behavior of the sensor at initial contact with the rigid base, while the second part involves FEA (finite element analysis) to describe the behavior of the sensor after initial contact, when the bilayer beam is pressed against the rigid base.

A. Beam Deflection at Initial Contact

1) Bilayer Beam Bending Stiffness: In order to describe the behavior of the bilayer beam and its deflection upon application of a force, its equivalent bending stiffness must first be expressed. For this, we use multilayer beam mechanics [34]. The equivalent bending stiffness D of a beam composed of n layers is given by Eq. (1), where E_i is the Young's modulus of the i-th layer, and I_i is its moment of inertia.

$$D = \sum_{i=1}^{n} E_i I_i, \qquad (1)$$

While the Young's modulus of the i-th layer only depends on the material of that particular layer, I_i depends on the location of the neutral fiber of the multilayer beam assembly, y_n [34], as visible in Fig. 2 in the case of 2 layers. The position of the neutral fiber is given by Eq. (2)

$$y_n = \frac{\sum_{i=1}^{n} B_i \delta_i + 2 \sum_{i=2}^{n} \left(B_i \sum_{j=1}^{i-1} \delta_j \right)}{2 \sum_{i=1}^{n} B_i}, \qquad (2)$$

where δ_i is the thickness of the i-th layer of the multilayer beam, and $B_i = E_i A_i$, with $A_i = \delta_i w$. The moment of inertia, I_i, of each layer is then computed using Eq. (3)

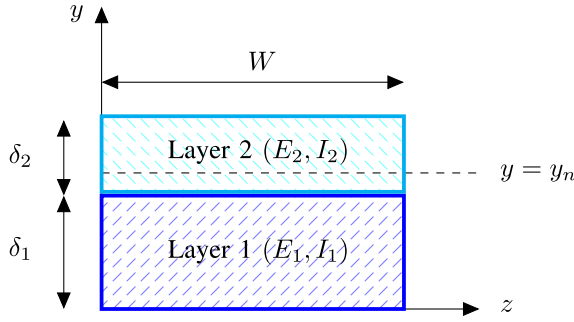$$I_i = \frac{W \delta_i^3}{12} + W \delta_i y^{*2}, \qquad (3)$$

Fig. 2. Schematic of a multilayer beam in the case of two layers, with the dimensions of its cross-section and the position of the neutral fiber y_n along the y-axis.

with

$$y^* = y_n - 0.5\delta_i - \sum_{m=1}^{i-1} \delta_m. \tag{4}$$

In the case of a beam composed of two layers (i.e. a bilayer beam), as is the case for our application, the bending stiffness, D, given by Eq. 1, reduces to Eq. 5.

$$D = W\left(\frac{E_1^2\delta_1^4 + 4E_1E_2\delta_1^3\delta_2 + 6E_1E_2\delta_1^2\delta_2^2 + 4E_1E_2\delta_1\delta_2^3 + E_2^2\delta_2^4}{I_2(E_1\delta_1 + E_2\delta_2)}\right) \tag{5}$$

2) Bilayer Beam Mechanics Model: In order to use the equations from beam mechanics, we assume that the beam satisfies Euler-Bernoulli's hypothesis. The hypothesis is satisfied if Eq. (6) holds, where E is the Young's modulus of the beam, I its cross-sectional moment of inertia, κ the Timoshenko shear coefficient, L the beam length, A its cross-sectional area, and G its shear modulus. In the case of a beam with a rectangular cross-section, $\kappa = 5/6$. For a bilayer beam, we assess the validity of Eq. (6) in the extreme case where the beam is comprised of two layers made (i) solely of material 1 and (ii) solely of material 2, which is sufficient to validate the hypothesis and covers all thickness ratios between these two extremes.

$$\frac{EI}{\kappa L^2 AG} \ll 1 \tag{6}$$

The deflection $y(x)$ of the bilayer beam subject to a point force is obtained by expressing the moment balance $M_z(x)$ along the bilayer beam in the regions $x \in [0, F_{loc}]$ and $x \in [F_{loc}, L]$ and calculating $\frac{d^2 y(x)}{dx^2} = \frac{M_z(x)}{D}$, and leads to the expressions in Eq. (7):

$$y(x) = \begin{cases} \dfrac{F_{mag}x^2(L - F_{loc})^2(Lx - 3LF_{loc} + 2F_{loc}x)}{6DL^3} \\ \qquad \text{if } x \in [0, F_{loc}] \\[2mm] \dfrac{F_{mag}F_{loc}^2(L - x)^2(LF_{loc} - 3Lx + 2F_{loc}x)}{6DL^3} \\ \qquad \text{if } x \in [F_{loc}, L], \end{cases} \tag{7}$$

with D the bending stiffness of the bilayer beam, given by Eq. (1). The maximum deflection y_{max} of the bilayer beam,
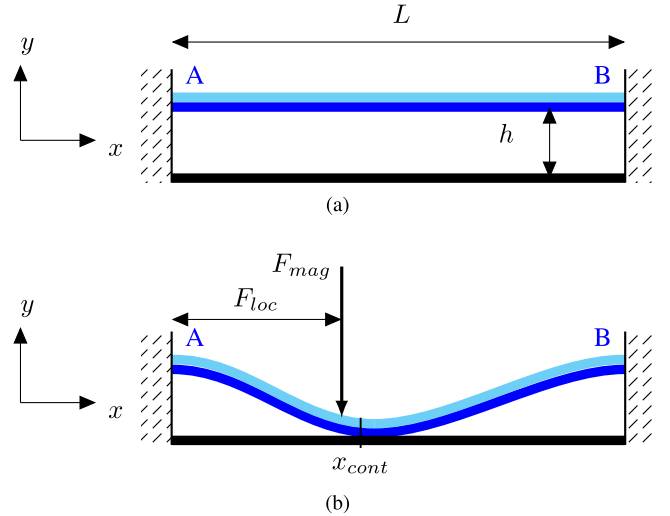

Fig. 3. Scheme of the bilayer sensor beam with double built-in supports, represented (a) at rest with its main physical parameters, and (b) at initial contact between the bilayer beam and the rigid base, with a force of magnitude F_{mag} exerted at location F_{loc}, leading to a single contact between the bilayer beam and the rigid base at $x = x_{cont}$.

and the location of this maximum deflection along it, are then obtained by solving $\frac{dy(x)}{dx} = 0$, leading to Eq. (8).

$$y_{max} = \begin{cases} \dfrac{2F_{mag}F_{loc}^2(L - F_{loc})^3}{3D(3L - 2F_{loc})^2} & \text{at } x = \dfrac{L^2}{3L - 2F_{loc}} \\ & \text{if } F_{loc} \leq L/2 \\[4mm] \dfrac{2F_{mag}F_{loc}^3(L - F_{loc})^2}{3D(L + 2F_{loc})^2} & \text{at } x = \dfrac{2LF_{loc}}{L + 2F_{loc}} \\ & \text{if } F_{loc} \geq L/2 \end{cases} \tag{8}$$

We can see that the two solutions in Eq. (8) are symmetric about $x = \frac{L}{2}$, by using the change of variable $F_{loc} \rightarrow L - F_{loc}$. Thus, only one half of the sensor needs to be studied, and we choose to consider forces applied to the first half ($F_{loc} \leq L/2$). The initial contact between the bilayer beam and the rigid base is obtained for a maximum deflection of the bilayer beam $y_{max} = h$ (see Fig. 3), which leads to Eq. (9) that must hold for $F_{loc} \leq L/2$.

$$h = \frac{2F_{mag}F_{loc}^2(L - F_{loc})^3}{3D(3L - 2F_{loc})^2} \tag{9}$$

Also, the contact location between the bilayer beam and the rigid base is at $x = x_{cont}$, with x_{cont} given by Eq. (10) (see Fig. 3(b)).

$$x_{cont} = \frac{L^2}{3L - 2F_{loc}} \tag{10}$$

As visible in Eq. (10), there is unicity between the contact location between the bilayer beam and the rigid base, x_{cont}, and the location of application of the force on it, F_{loc}, which allows a unique mapping between them. Then, we observe that for a particular sensor, as F_{loc} decreases to 0, F_{mag} must tend to infinity for Eq. (9) to hold, which means that the proposed mechanical transducer has edge effects. To ensure that forces of a given magnitude can be sensed, Eq. (9) must be verified for the smallest values of F_{loc}. In addition, Eq. (9) allows
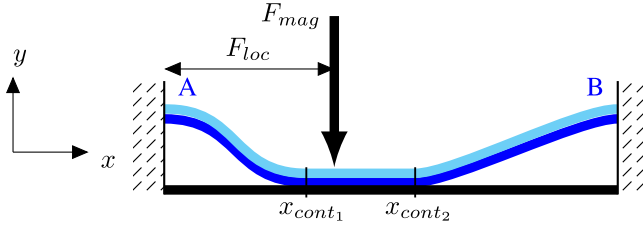
Fig. 4. Scheme of the bilayer sensor beam with double built-in supports after initial contact, when a force of F_{mag} is applied at location F_{loc}. The edges of the contact locations are denoted x_{cont_1} and x_{cont_2}.

us to define a relationship between the minimum force that can be sensed by the sensor and all of its mechanical design parameters, which is suitable for design optimization purposes. Indeed, the bilayer beam deflection for initial contact, h, is an increasing function of L and a decreasing function of D, and therefore a decreasing function of W, E_1, E_2, δ_1, δ_2. By adjusting these design variables, desired performance can be obtained in terms of the minimum force that can be detected along the sensor length.

B. Beam Deformation After Initial Contact

After initial contact, as both beams are pressed against each other, beam mechanics is no longer applicable, and finite element analysis is thus used to model the contact between them. FEA is used to compute the location of the contact edges x_{cont_1} and x_{cont_2} between the bilayer beam and the rigid base, as illustrated in Fig. 4. An increase in applied force corresponds to an increase in contact length between the beams around the initial contact point predicted by the bilayer beam mechanics model. A critical requirement for the sensor is that the displacement of these contact edges should lead to significant phase changes that are measurable and provide sufficient force magnitude and application location resolution. The contact edge location requirements are thus dictated by the next sections on the trace design and wireless phase measurement approach. They will lead to the selection of the design parameters L, w, E_1, E_2, δ_1, δ_2 and h of the sensor that, while respecting Eq. (8), will allow us to obtain the desired contact edges between the bilayer beam and the rigid base.

IV. ELECTRICAL TRACE DESIGN

In this section, we present the design rules that dictate the geometry of the signal trace of the sensor, which is used to convert the mechanical contact between the beams into phase changes of the electromagnetic waves that travel along it. The case of a rectilinear signal trace, which connects both ends of the sensor along a straight line, is considered in this work.

1) Sensor Impedance: In order for the sensor to be compatible with connected electrical components, i.e. antennas, it must match the impedance of such components. A common, widely adopted standard is an impedance of 50 Ω, so the sensor is designed to match this value. The sensor can be seen as analogous to two parallel microstrips, separated by a dielectric – in this case, air. With such a representation, the impedance of the sensor has a known expression presented in [35], and given by Eq. (11) in the case of a material that has a dielectric
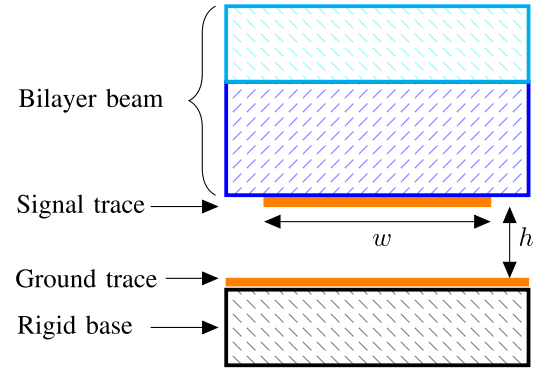

Fig. 5. Representation of the signal and ground traces covering the bilayer beam and rigid base, respectively, with the design parameters represented for the signal trace.

constant close to 1, which is the case for air:

$$Z = 60 \ln \left(\frac{F_1 h}{w} + \sqrt{1 + \left(\frac{2h}{w} \right)^2} \right), \tag{11}$$

with $F_1 = 6 + (2\pi - 6) \exp(-(30.666 \frac{h}{w})^{0.7528})$. As visible in Eq. (11), the sensor impedance is a function of the signal trace width, w, and the spacing between the signal and ground trace, h, that must be adjusted to obtain a desired impedance of 50 Ω.

2) From Contact Location to Phase Change: The role of the electrical trace is to convert the locations of the contact edges between the bilayer beam and the rigid base to phase values. Indeed, the phase shifts measured on both ends of the sensor are a function of the length traveled by the electromagnetic wave in the trace. Matching the sensor impedance as described in the previous section ensures that we obtain a linear relationship between the length traveled by the wave on the signal trace and the phase that it accumulates in the process. Generally, this linear relationship between phase and length travelled, l, is given by Eq. (12)

$$\Delta \phi = \gamma \, \Delta x, \quad \text{with} \quad \gamma = \frac{2\pi f}{c}, \tag{12}$$

where c is the celerity of the electromagnetic wave in the signal trace, and f its frequency. However, when the force sensor is pressed, the separation between the signal trace and ground trace tapers down from height h to 0 at the contact point. For such tapered transmission lines, the propagation exponent has the form of $(1 - e^{-\gamma \Delta x})$ [36], which has a phase of $-\frac{\gamma}{2} \Delta x$, instead of $-\gamma \Delta x$ for parallel transmission lines. This leads to the new relationship $\Delta \phi = \frac{\gamma}{2} \Delta x$. Finally, the phase accumulated for a displacement of a contact edge between the traces of Δx must be doubled, as the wave follows the path once, is reflected at the shorting location, and travels back along the same path. Simplifying the coefficients results in the relationship between the contact edge displacement and the measured phase, as given by Eq. (13).

$$\Delta \Phi = \left(\frac{2\pi f}{c} \right) \Delta x \tag{13}$$

Lastly, to ensure unicity of the phase measurement, the length of the signal trace must be limited to the wavelength of the signal that travels along it. Thus, the maximum signal trace

length, which is also the maximum bilayer beam length, L_{max}, is given by Eq. (14). This relationship is a design rule that must hold for both the trace and the bilayer beam length.

$$L_{max} = \frac{1}{2}\left(\frac{c}{f}\right) \tag{14}$$

V. WIRELESS PHASE MEASUREMENT

In this section, we propose an approach to sense the phases of the signal wirelessly on both sides of the sensor, using backscattering.

A. Measuring the Signal Reflected by the Sensor

To perform backscattered phase measurements, a wireless reader, equipped with both a transmit antenna and a receive antenna, is used. The reader transmits an excitation signal, $s(t)$, which is received and reflected by the sensor. A summation of both the reflected signal, as well as the excitation signal, are then read at the receive antenna. The signal reflected by the sensor must first be distinguished from the excitation signal. To achieve this, the signal received by the sensor is modulated with a low power On-Off Keying (OOK) modulation, before being reflected back. This approach is popular for RFID and backscatter systems [37]–[39]. It consists of a multiplication of the reflected signal by a square wave of frequency $f_s = \frac{1}{T_s}$, where T_s is its on-off time period. The reflected signal, $r(t)$, after OOK modulation of $s(t)$ is therefore given by $r(t) = m(t)s(t)$, where $m(t)$ is given by Eq. (15).

$$m(t) = \begin{cases} 0, & nT_s \leq t < (nT_s + \frac{T_s}{2}) \\ 1, & (nT_s + \frac{T_s}{2}) \leq t < (n+1)T_s, n \in \mathbb{Z} \end{cases} \tag{15}$$

Expanding $m(t)$'s Fourier series, the sum of the odd harmonics is obtained using Eq. (16).

$$m(t) = \sum_{k \in (2i+1), i \in \mathbb{Z}} \frac{1}{|k|} e^{(j2\pi k f_s t)} \tag{16}$$

Ignoring the weaker high order harmonics, the reflected $r(t)$ is given by Eq. (17).

$$r(t) = s(t)m(t) \approx s(t)e^{j2\pi f_s t} \tag{17}$$

This approach leads to the reflected signal being shifted in the frequency domain by f_s, the frequency of the square wave, thus isolated the reflected signal from the emitted signal. In order to measure the phase changes on both ends of the signal trace independently, without interference from the opposite end, RF switches on both ends of the sensor are toggled at different frequencies f_{s_1}, f_{s_2}. The signals reflecting from the two ends of the sensor thus give the accumulated phases ϕ_1, ϕ_2, in addition to the modulations at frequencies f_{s_1} and f_{s_2}.

B. Measuring the Phases of Interest

Once the signal reflected by the sensor can be measured by the reader, the next step is to extract the phases of the signals reflected at the shorting locations of the signal and ground trace of the sensor. When a force acts on the sensor and the bilayer beam touches the rigid base between the contact locations $x_{cont_{1,2}}$, the phases measured by the reader are a sum
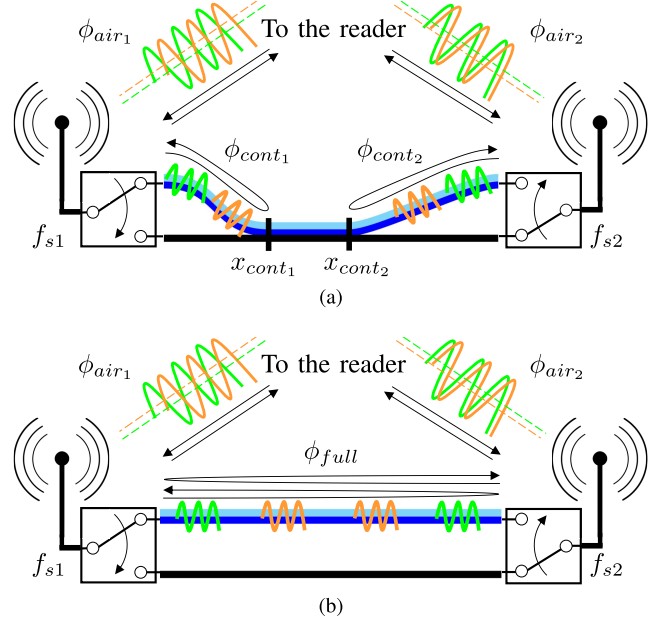

Fig. 6. Working principal of the wireless phase sensing approach, with (a) the sensor pressed, with the phases ϕ_{cont_1}, ϕ_{cont_2} and ϕ_{air} represented, and (b) the sensor represented at rest and the phases ϕ_{full} and ϕ_{air} labeled.

of two phases, $\phi_{air_{1,2}}$ and $\phi_{cont_{1,2}}$, as illustrated in Fig. 6(a). The phases $\phi_{air_{1,2}}$ are due to the presence of air between the sensor and the reader. The phases of interest, $\phi_{cont_{1,2}}$, are due to the signals that travel from end 1 and 2 of the sensor, respectively, until the contact edges, and reflect back from there. They are given by Eq. (19).

$$\phi_{cont_1} = \left(\frac{2\pi f}{c}\right) x_{cont_1}, \quad \phi_{cont_2} = \left(\frac{2\pi f}{c}\right) x_{cont_2} \tag{19}$$

This leads to total phases measured at both ends of the sensor given by Eq. (20).

$$\begin{cases} \phi_{force_1} = \phi_{air_1} + \phi_{cont_1}, \\ \phi_{force_2} = \phi_{air_2} + \phi_{cont_2} \end{cases} \tag{20}$$

As visible in Eq. (20), the phases of interest $\phi_{cont_{1,2}}$ cannot be measured directly, as they are added to the phases due to the presence of air between the sensor and the reader. In order to cancel these added phases, a differential measurement is performed between the sensor pressed and the sensor at rest. Indeed, when no force is applied on the sensor, phases $\phi_{noforce_{1,2}}$ are measured at both ends, as illustrated in Fig. 6(b). These phases are given by Eq. (21).

$$\begin{cases} \phi_{noforce_1} = \phi_{air_1} + \phi_{full}, \\ \phi_{noforce_2} = \phi_{air_2} + \phi_{full}, \end{cases} \tag{21}$$

with ϕ_{full} a constant given by Eq. (22).

$$\phi_{full} = \left(\frac{2\pi f}{c}\right) L \tag{22}$$

By measuring the phase changes (i.e. the difference between the phase measured by the reader before and after a force is applied), the phases due to the presence of air between the

TABLE II
MECHANICAL CHARACTERISTICS OF THE BILAYER
BEAM OF THE SENSOR

Parameter	Bottom layer (#1)	Top layer (#2)
Material	Ecoflex 00-30	Acrylic
Young modulus E (Pa)	125×10^3	2×10^9
Poisson's Ratio	0.49	0.35
Thickness δ (mm)	2.54	1.4
Width W (mm)		9.85
Length L (mm)		80
Spacer height h (mm)		0.64
Trace width w (mm)		2.5

sensor and the reader are canceled, as shown in Eq. (23).

$$\begin{cases} \phi_{noforce_1} - \phi_{force_1} = \phi_{full} - \phi_{cont_1} = \phi_1, \\ \phi_{noforce_2} - \phi_{force_2} = \phi_{full} - \phi_{cont_2} = \phi_2, \end{cases} \quad (23)$$

Hence, the additional phase due to the presence of air can be removed, and the desired phase information can be obtained, enabling the measurement of the phases due to the displacement of the shorting points on the signal trace (please refer to [40] for more details on the wireless implementation).

VI. APPLICATION AND FABRICATION

In this section, we apply the design rules and principles presented for the mechanical, electrical and wireless components, and implement a sensor that meets desired requirements.

We start by selecting a frequency for the sensor. As visible in Eq. (13), the frequency of the sensor should be maximized in order to accumulate the maximum phase change on both ends of the sensor, and thus increase the resolution. Our focus here is on medical applications, where signal losses increase as a wave goes trough human tissue for frequencies higher than 1 GHz [41], [42]. Hence, we select a frequency (f) equal to 915 MHz in this work. The choice of frequency also allows us to compute the maximum signal trace and bilayer beam lengths to avoid phase redundancy measurements, as given by Eq. (14). For a frequency of $f = 915$ MHz and a celerity of wave in the electrical trace, c, approximated by the speed of light in the void (299×10^6 m/s), we obtain a maximum length of $L_{max} = 164$ mm, that must hold for the sensor.

The next step in the design process is the mechanical implementation. For this work, we aim to sense forces between 2 and 8 N, on 50% of its length. Because the sensor is less sensitive close to its edges, as detailed in Section III, we center this area in the middle of the sensor, at $x = L/2$. As the maximum deflection of the sensor is an increasing function of F_{loc} (for $F_{loc} \leq L/2$), the critical location to ensure a minimum force detection of 2 N is at $F_{loc} = L/4$. By replacing F_{mag} with 2 N and F_{loc} with $L/4$ in Eq. (9), the design rule that must be respected for our prototype is then given by Eq. (23), shown at the bottom of the page.

We select mechanical components with characteristics reported in Table II, with acrylic for the top layer and Ecoflex 00-30 for

the bottom layer of the bilayer beam. These parameters allow Euler-Bernoulli's hypothesis to be respected, with a bilayer beam solely made out of the material of layer 1 (leading to $0.00074 \ll 1$) and a bilayer beam solely mode out of the material of layer 2 (leading to $0.00067 \ll 1$) (see Eq. (6)). They also verify Eq. (23), and we have $L < L_{max}$. The predicted forces at initial contact as well as the location of the initial contact along the sensor are represented in the second row of Table III by black points. For the force application locations of 20, 30, 40, 50 and 60 mm along the sensor, the forces for initial contact are 2.00, 1.25, 1.08, 1.25 and 2.00 N, respectively, which satisfy the requirements in terms of minimum force to be sensed, and the contact locations are 32, 35.6, 40, 44.4 and 48 mm, respectively.

We then use FEA to quantify the locations of the contact edges between the beams as a force is applied to it, to ensure that a significant phase change can be obtained. For this purpose, we used COMSOL Multiphysics (COMSOL, Inc., Burlington, USA) to model the sensor beams and perform the analysis. The bottom layer of the bilayer beam, made out of Ecoflex 00-30, is modeled using the hyperelastic Yeoh model, with $C_1 = 17$ KPa, $C_2 = -0.2$ KPa and $C_3 = 0.023$ kPa [43]. The initial bulk modulus is computed using the relationship $K = \frac{E}{3(1-2v)}$, with a Poisson's ratio of 0.49. The locations of the applied forces are 20, 30, 40, 50 and 60 mm, and the force magnitude for each location is varied between 0 and 8 N in 0.1 N increments. The resulting bilayer beam shapes for initial contact, 4 N, and 8 N of applied force are visible in the first row of Table III. As visible in Table III, the contact length increases when the force applied on the beam increases, and goes from a single initial contact point to a contact length (computed as $x_{cont_2} - x_{cont_1}$) of 28.7 mm on average for all force locations assessed, for a force of 8 N. This phenomenon is also visible in all the plots in the second row of Table III, which represents the location of the contact edges between the bilayer beam and the rigid base, as the force magnitude increases. Using Eq. (13), this variation of overall contact length of 28.7 mm corresponds to an accumulated phase change of 31.5 degrees, which means approximately 4 degrees/N, which is a satisfactory resolution, thus validating the mechanical design.

The last implementation step is the design of the electrical trace. Using Eq. (11) with a desired impedance of $Z = 50 \Omega$ and a spacer height of $h = 0.64$ mm, the trace width is computed to be 4.75 mm. However, because the dielectric between the signal and ground trace is not only made of air, since plastic spacers separate the traces at both ends of the sensor, we found that a lower value of 2.5 mm works better in practice. This is thus the adopted value in our design.

A picture of the fabricated sensor is visible in Fig. 7, with labels for each component. The top layer was laser-cut from an acrylic sheet with the desired thickness. The bottom layer was created by molding Ecoflex 00-30 between two acrylic sheets

$$h = \frac{27L^3(E_1\delta_1 + E_2\delta_2)}{400W(E_1^2\delta_1^4 + 4E_1E_2\delta_1^3\delta_2 + 6E_1E_2\delta_1^2\delta_2^2 + 4E_1E_2\delta_1\delta_2^3 + E_2^2\delta_2^4)} \quad (23)$$

TABLE III

FIRST ROW: REPRESENTATION OF THE BILAYER BEAM SHAPE OBTAINED USING FEA, FOR A FORCE LEADING TO INITIAL CONTACT WITH THE RIGID BASE, 4 N, AND 8 N. SECOND ROW: THEORETICAL RESULTS GIVEN BY BILAYER BEAM MECHANICS, LOCATION OF THE CONTACT EDGES BETWEEN THE BEAMS GIVEN BY FEA, OVERLAYED WITH THE RESULTS OF THE MECHANICAL TESTINGS

USA) onto a 0.1 mm thick plastic film that was glued onto the bottom side of the Ecoflex 00-30 layer with cyanoacrylate. The ground trace was fabricated using copper tape with a width of 6.4 mm and a thickness of 0.06 mm, applied directly onto the rigid base, and SMA connectors were soldered on both ends of the traces, as visible in Fig. 7(b), to allow an electrical access to them by the switches and the antenna.

VII. EXPERIMENTAL EVALUATION

In this section, we conduct experimental evaluations of the proposed sensor, including validation of the mechanical behavior, the length to phase conversion of the electrical trace using a wired experiment, and, finally, the overall wireless sensor.

A. Mechanical Performance

We first evaluate the mechanical performance of the bilayer beam, to ensure that the contact length between the bilayer beam and the rigid base matches both the bilayer beam mechanics model and the results of the FEA. For this purpose, we used the experimental setup shown in Fig. 8. It consists of the bilayer beam onto which the signal trace is attached, along with a linear actuator equipped with an indenter to press on the sensor at specified locations. The rigid base of the sensor is replaced with a PCB that includes 112 parallel, equally spaced conducting traces, connected at their ends in a zig-zag manner through resistors in series. The distance between each conducting trace is 0.5 mm, and the values of the resistors is 100 Ω. When the bilayer beam touches the PCB, the contact edges between the bilayer beam and the PCB can be determined by measuring the voltage in the circuit
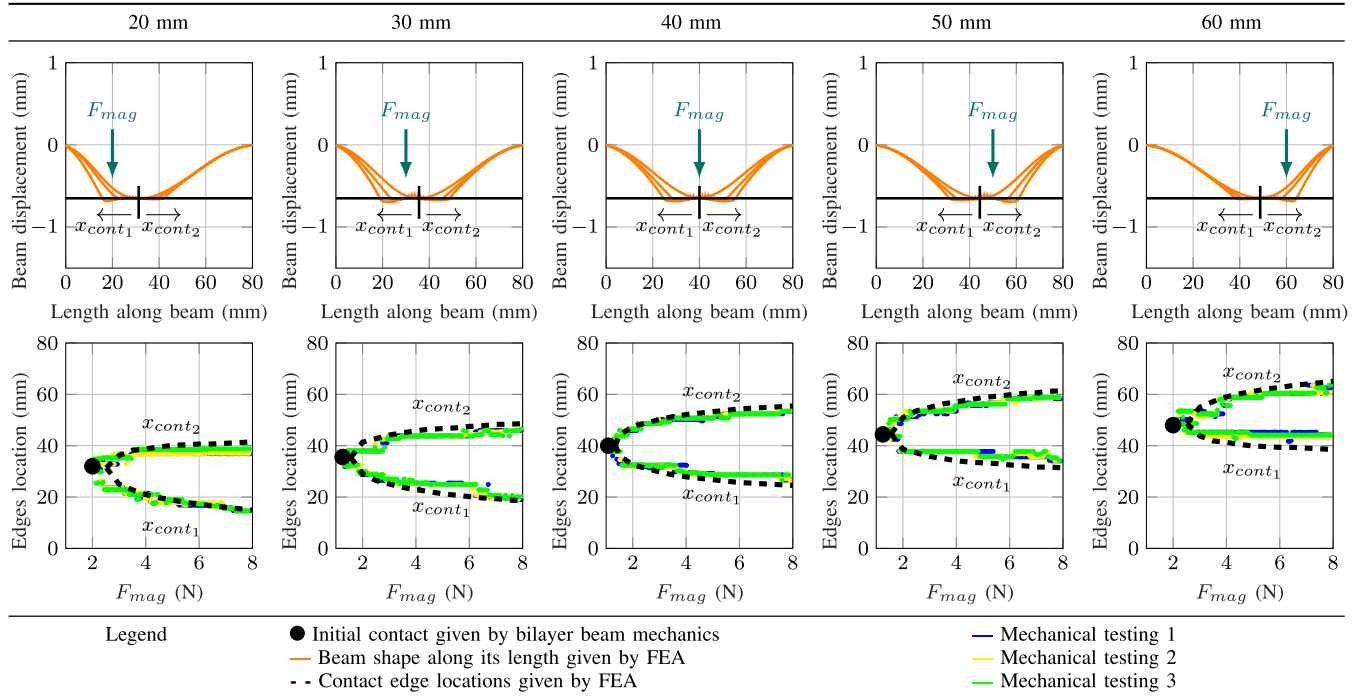

Fig. 7.   Pictures of the fabricated sensor, with (a) a side view with the top and bottom layers of the bilayer beam labeled, as well as the rigid base and the spacers, and (b) a top view with the signal and ground traces visible in transparency, the SMA connectors that allow access to the signal and ground traces, and the sensor support.

spaced by 2.54 mm. These two fabricated layers were then glued together with cyanoacrylate, and are visible in Fig. 7(a). The signal trace was fabricated by applying a thickness of 0.06 mm of Fast Drying Silver Paint (Ted Pella, Inc., CA,

TABLE IV
WIRED MEASUREMENTS OF PHASES ϕ_1 AND ϕ_2 ON BOTH ENDS OF THE SENSOR USING THE VNA VERSUS THE FORCE F_{mag} APPLIED ON IT, FOR ALL 3 TRIALS PERFORMED
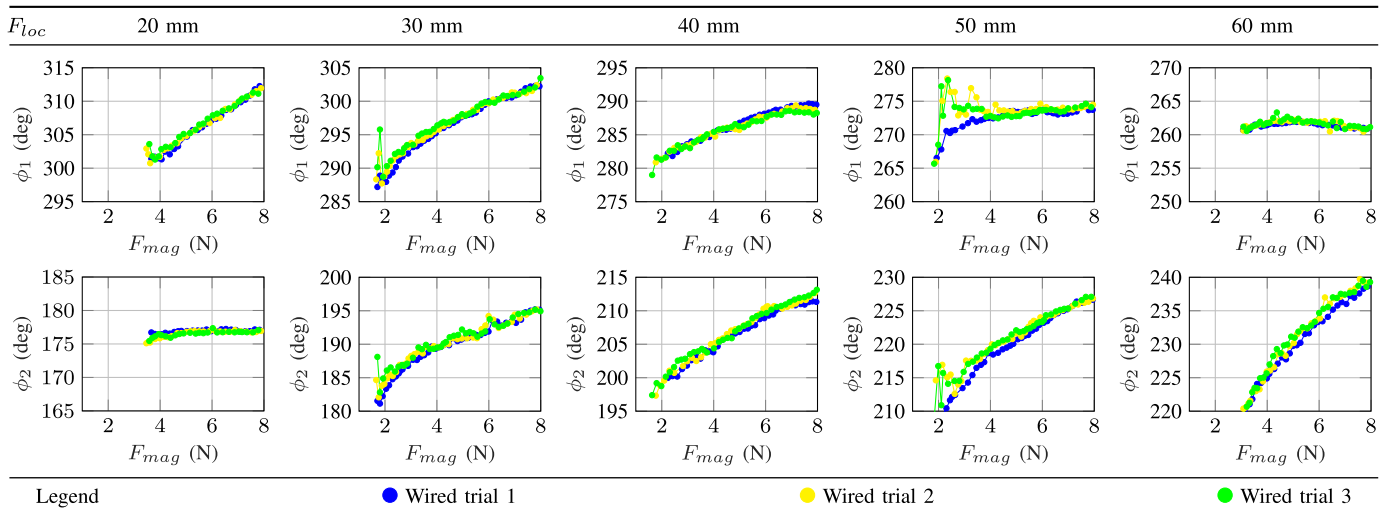

Fig. 8. Experimental setup for assessment of the mechanical performance, with the rigid base of the sensor replaced by a PCB, and a linear actuator equipped with an indenter to press on the sensor. The sensor and PCB are attached on a base that is mounted on a load cell to have ground truth force magnitude measurements.

Fig. 9. Experimental setup for wired measurements, with the VNA, load cell, sensor, and linear actuator equipped with an indenter.

on both ends. A load cell located under the PCB measures the forces applied to the sensor. To ensure that the spacing between the bilayer beam and the PCB is the same as that between the bilayer beam and the rigid base in the designed sensor, it was measured by placing the indenter in contact with the bilayer beam using the load cell to detect it, and counting the number of steps required to short the signal trace and the PCB. The measured spacing was 0.65 mm, which is close to the desired value of 0.64 mm. The following experiment was then conducted: for locations 20, 30, 40, 50 and 60 mm along the beam, a force is applied and gradually increased from 0 to 8 N. The experiment is repeated 3 times for each location.

The results are visible in the second row of Table III, where the green, yellow and blue lines represent the location of the contact edges between the bilayer beam and the PCB for each trial as the force magnitude increases. As visible in this table, the conditions for initial contact between the bilayer beam and the PCB are close to the ones given by the bilayer beam mechanics model and the FEA, both in terms of the location of first contact and the required force magnitude.
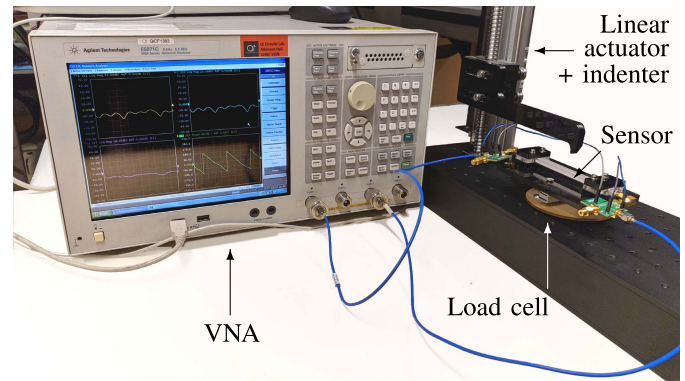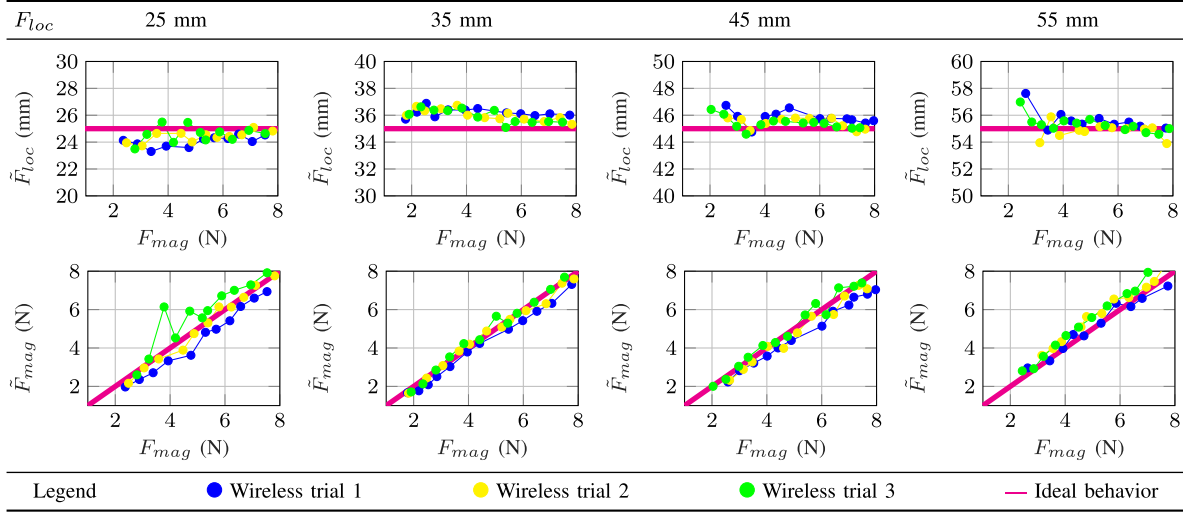
TABLE V
COEFFICIENTS OF THE POLYNOMIAL FUNCTION FOR f_{mag} AND f_{loc} IDENTIFIED USING THE COLLECTED WIRED DATA

Coefficient	f_{mag}	f_{loc}
$a_{0,0}$	8886	368
$a_{1,0}$	-67.81	9.794
$a_{0,1}$	-28.07	-16.23
$a_{2,0}$	0.1676	-0.05639
$a_{1,1}$	0.1585	0.03538
$a_{0,2}$	0.01207	0.06403
$a_{3,0}$	-0.000133	6.983×10^{-5}
$a_{2,1}$	-0.0002158	2.319×10^{-5}
$a_{1,2}$	-5.472×10^{-5}	-0.0001222
$a_{0,3}$	1.692×10^{-5}	-5.891×10^{-5}

Indeed, the average error on the location of the first contact is 1.77 mm and 1.76 mm for the bilayer beam mechanics model and the FEA model, respectively, and 0.09 N and 0.29 N for the bilayer beam mechanics model and the FEA model, respectively. Finally, the obtained length of the bilayer beam in contact with the rigid base ($x_{cont_2} - x_{cont_1}$) for $F_{mag} = 8$ N is 28.7 mm in the case of the FEA and 23.7 mm for the experiments. This difference of 5 mm remains reasonable considering possible modeling and manufacturing errors of

TABLE VI

ESTIMATED FORCE MAGNITUDES $\tilde{F}_{mag}$ AND LOCATIONS $\tilde{F}_{loc}$ GIVEN BY THE WIRELESS SENSOR FOR THE 3 TRIALS PERFORMED AS A FUNCTION OF THE FORCE F_{mag} APPLIED ON IT, MEASURED WITH THE LOAD CELL. THE IDEAL WIRELESS FORCE SENSOR RESULTS FOR THE LOCATION AND MAGNITUDE ARE OVERLAID IN MAGENTA

the sensor. A contact length of 23.7 mm still gives an expected phase change of 26.0 degrees, which can still be detected by the wireless phase sensing approach. This validates the mechanical behavior of the bilayer beam.

B. Wired Performance and Sensor Model

In order to have ground truth data of the contact edge location to phase conversion given by the electrical trace, we collect wired measurements of the sensor under applied loads. For this purpose, we use the experimental setup visible in Fig. 9. It is composed of the sensor attached to a load cell that provides ground truth force measurements, and a linear actuator equipped with an indenter that presses down on the sensor at desired locations. Both ends of the sensor are connected to a VNA (Vector Network Analyzer) that allows us to measure phases on the signal trace in a wired configuration. We replaced the PCB used in the mechanical testing with the rigid base and ground trace of the designed sensor. We again verified the spacing between the bilayer beam and the rigid base by placing the indenter in contact with the beam using the load cell readings, and moving it down until the signal and ground traces were shorted. The measured spacer height was 0.63 mm, which is sufficiently close to the desired value of 0.64 mm. Forces are applied at locations 20, 30, 40, 50 and 60 mm and are gradually increased from 0 to 8 N. This experiment is repeated 3 times, and for each force value, phases are measured and recorded on both ends of the sensor.

The results, as visible in the graphs of Table IV, illustrate the repeatability of the phase changes. The exception are the results at 50 mm, which are less repeatable for forces between 2 and 3 N, likely due to a local non-planarity of the sensor components, leading to a contact length that is increasing rapidly as the force magnitude increases. We also observe that, for a given location along the sensor, the sum of the phase amplitude changes measured on both sides of the sensor equals 21.2 degrees on average, which is in accordance with the expectation of 26.0 degrees for a average contact lengths

of 23.7 mm observed during the mechanical testings. The wired measurements obtained are thus satisfactory.

We then use these phases measured in a wired configuration, namely ϕ_1 and ϕ_2, to compute a model that estimates the force magnitude and application location based on a given phase change. For this, we perform an interpolation of the force magnitude, as measured by the load cell, and application location using a polynomial of degree 3 in both ϕ_1 and ϕ_2. We then obtain a functional approximation of the force magnitude, $\tilde{F}_{mag}$, and application location, $\tilde{F}_{loc}$, from the measured phases and given by Eq. (24).

$$
\begin{aligned}
\tilde{F}_{mag,loc} &= f_{mag,loc}(\phi_1, \phi_2) \\
&= a_{0,0} + a_{1,0}\phi_1 + a_{0,1}\phi_2 + a_{2,0}\phi_1^2 + a_{11}\phi_1\phi_2 \\
&\quad + a_{0,2}\phi_2^2 + a_{3,0}\phi_1^3 + a_{2,1}\phi_1^2\phi_2 + a_{1,2}\phi_1\phi_2^2 + a_{0,3}\phi_2^3
\end{aligned}
$$
(24)

The coefficients identified using the collected wired data are reported in Table V. These functional approximations lead to RMS errors of 0.13 N for the force magnitude, and 0.25 mm for the force application location. We validate these models using new data collected at a location of 55 mm. The obtained RMS errors for the force magnitude and application location are 0.57 N and 0.23 mm, respectively, which validates the models.

C. Assessment of the Overall Wireless Performance

Finally, we assess the performance of the sensor in a wireless configuration, using the approach presented in Section V. For this purpose, the setup visible in Fig. 10 is used. It is composed of the sensor attached to the load cell and the linear actuator with the indenter to press on it at desired locations. Each end of the sensor is connected to a switch for the OOK approach, and each of the two switches are connected to an antenna. Two additional antennas, a transmitter and a receiver, are used to send a signal to the sensor antenna and to read the reflected signal, respectively. Forces are applied at
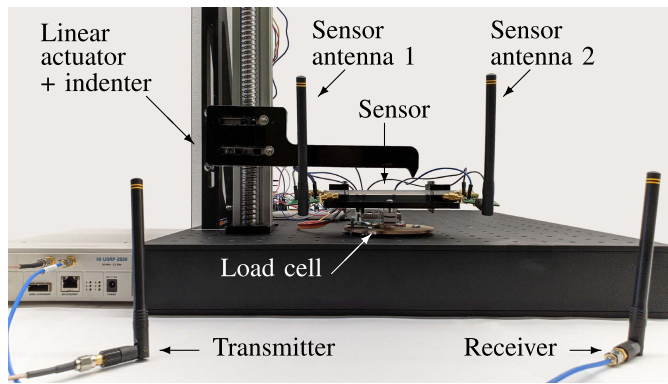
Fig. 10. Experimental setup for wireless testing, including the sensor and its antenna, load cell, linear actuator with the indenter, and the antennas of the reader.

locations 25, 35, 45 and 55 mm along the sensor to assess the performance of the sensor at different, intermediate locations compared to the wired experiment, for which the sensor model was created. The force magnitude is gradually increased from 0 to 8 N for each of these locations.

Table VI shows the force magnitudes and locations $\tilde{F}_{mag}$ and $\tilde{F}_{loc}$ given by the sensor, for all 3 trials performed. These are obtained by using the model in Eq. (24) with coefficients reported in Table V, on the phases measured wirelessly. As visible in this table, the measurements are repeatable, and close to the expected, ideal behavior. The average error and standard deviation between the sensors readings $\tilde{F}_{mag}$ and the load cell readings F_{mag} are 0.01 N and 0.49 N, respectively, while the average error and standard deviation between the sensor readings $\tilde{F}_{loc}$ and the force application locations are -0.33 mm and 0.82 mm, respectively. These errors are orders of magnitude lower than the sensor length and range of detectable forces, thus validating the feasibility of the proposed sensor concept and implementation.

VIII. CONCLUSION

In this paper, we presented a new force sensor based on wave backattering. The design rules of the mechanical transducer, based on a bilayer beam, were presented. The design rules of the electrical trace, on which electromagnetic waves travel and get reflected, were also detailed, as was a method to sense changes in the phase of the reflected signal, wirelessly. An implementation of the sensor was proposed, and a prototype was then fabricated. Experimental validations of this prototype were conducted to validate its mechanical performance and its ability to sense phase changes with both a wired and wireless connection. The experiments showed satisfactory initial results, with a range of force magnitude between 2 N and 8 N that can be sensed on 50% of the sensor length, with an average error and standard deviation on the force magnitude of 0.01 N and 0.49 N, respectively, and an average error and standard deviation on the force location of -0.33 mm and 0.82 mm, respectively.
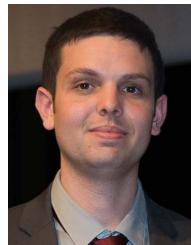
Future work will be focused on the miniaturization of the force sensor to make it compatible with the dimensions of medical tools and continuum robots, which motivate its development. To achieve this goal, size constraints posed by the off-the-shelf components (RF switches and antennas) will be removed through the integration of custom backscatter RFIC [44] solutions. The sensor itself can also be miniaturized by considering meander signal traces [45] and other geometries, instead of a straight line signal trace as in the current sensor prototype. In addition, alternative manufacturing technologies of the sensor components will be investigated in order to produce and assemble the mechanical and electrical parts at a smaller scale. The exploration of various sensor shapes and flexible designs will be conducted for integration on tubular, compliant surgical instruments. Extending the force range that can be sensed by the sensor and increasing the accuracy of the measurements will also be the object of future work. Also, the integration of multiple sensors for the sensing of a larger surface, as well as simultaneous reading of force information from multiple sensors, is of interest and will be assessed. In addition, the use of various frequencies, based on the applications, will be investigated. Finally, we plan on making passive sensors by using energy harvesting to power the switches present on the sensor, which are the only components that require an external source of energy in the current prototype.

REFERENCES

[1] A. M. Almassri *et al.*, "Pressure sensor: State of the art, design, and application for robotic hand," *J. Sensors*, vol. 2015, Jul. 2015, Art. no. 846487.

[2] R. D. D'Souza, A. Joshy, and A. Mini, "The art of tactile sensing: A state of art survey," *Int. J. Sci.*, vol. 26, no. 3, p. 16, 2016.

[3] C. Chi, X. Sun, N. Xue, T. Li, and C. Liu, "Recent progress in technologies for tactile sensors," *Sensors*, vol. 18, no. 4, p. 948, Mar. 2018. [Online]. Available: http://www.mdpi.com/1424-8220/18/4/948

[4] Y. Al-Handarish *et al.*, "A survey of tactile-sensing systems and their applications in biomedical engineering," *Adv. Mater. Sci. Eng.*, vol. 2020, Jan. 2020, Art. no. 4047937. [Online]. Available: https://www.hindawi.com/journals/amse/2020/4047937/

[5] A. M. Okamura, "Haptic feedback in robot-assisted minimally invasive surgery," *Current Opinion Urol.*, vol. 19, no. 1, p. 102, 2009.

[6] J. Burgner-Kahrs, D. C. Rucker, and H. Choset, "Continuum robots for medical applications: A survey," *IEEE Trans. Robot.*, vol. 31, no. 6, pp. 1261–1280, Dec. 2015.

[7] P. Polygerinos, D. Zbyszewski, T. Schaeffter, R. Razavi, L. D. Seneviratne, and K. Althoefer, "MRI-compatible fiber-optic force sensors for catheterization procedures," *IEEE Sensors J.*, vol. 10, no. 10, pp. 1598–1608, Oct. 2010.

[8] F. Taffoni, D. Formica, P. Saccomandi, G. Pino, and E. Schena, "Optical fiber-based MR-compatible sensors for medical applications: An overview," *Sensors*, vol. 13, no. 10, pp. 14105–14120, Oct. 2013.

[9] C. Shi *et al.*, "Shape sensing techniques for continuum robots in minimally invasive surgery: A survey," *IEEE Trans. Biomed. Eng.*, vol. 64, no. 8, pp. 1665–1678, Aug. 2017.

[10] Y. Noh *et al.*, "A three-axial body force sensor for flexible manipulators," in *Proc. IEEE Int. Conf. Robot. Autom. (ICRA)*, May 2014, pp. 6388–6393.

[11] Y. Noh *et al.*, "A continuum body force sensor designed for flexible surgical robotics devices," in *Proc. 36th Annu. Int. Conf. IEEE Eng. Med. Biol. Soc.*, Aug. 2014, pp. 3711–3714.

[12] Y. Noh *et al.*, "Multi-axis force/torque sensor based on simply-supported beam and optoelectronics," *Sensors*, vol. 16, no. 11, p. 1936, Nov. 2016.

[13] Y. Noh, S. Han, P. Gawenda, W. Li, S. Sareh, and K. Rhode, "A contact force sensor based on S-Shaped beams and optoelectronic sensors for flexible manipulators for minimally invasive surgery (MIS)," *IEEE Sensors J.*, vol. 20, no. 7, pp. 3487–3495, Apr. 2020.

[14] S. C. Ryu and P. E. Dupont, "FBG-based shape sensing tubes for continuum robots," in *Proc. IEEE Int. Conf. Robot. Autom. (ICRA)*, May 2014, pp. 3531–3537.

[15] R. Xu, A. Yurkewich, and R. V. Patel, "Curvature, torsion, and force sensing in continuum robots using helically wrapped FBG sensors," *IEEE Robot. Autom. Lett.*, vol. 1, no. 2, pp. 1052–1059, Jul. 2016.

[16] T. Chen *et al.*, "Novel, flexible and ultra-thin pressure feedback sensor for miniaturized intra-ventricular neurosurgery robotic tools," *IEEE Trans. Ind. Electron.*, early access, Apr. 9, 2020, doi: 10.1109/TIE.2020.2984427.

[17] M. Sim *et al.*, "Psychological tactile sensor structure based on piezoelectric sensor arrays," in *Proc. IEEE World Haptics Conf. (WHC)*, Jun. 2017, pp. 340–345.

[18] E. Lou, V. J. Raso, B. Martin, M. Epper, and D. L. Hill, "A wireless load measurement tool for spine surgery," in *Proc. IEEE Instrum. Meas. Technol. Conf.*, vol. 3, May 2005, pp. 1813–1817.

[19] C. Li *et al.*, "Review of research status and development trends of wireless passive LC resonant sensors for harsh environments," *Sensors*, vol. 15, no. 6, pp. 13097–13109, Jun. 2015.

[20] E. L. Tan, B. D. Pereles, R. Shao, J. Ong, and K. G. Ong, "A wireless, passive strain sensor based on the harmonic response of magnetically soft materials," *Smart Mater. Struct.*, vol. 17, no. 2, Apr. 2008, Art. no. 025015.

[21] Q.-A. Huang, L. Dong, and L.-F. Wang, "LC passive wireless sensors toward a wireless sensing platform: Status, prospects, and challenges," *J. Microelectromech. Syst.*, vol. 25, no. 5, pp. 822–841, Oct. 2016.

[22] S. Pradhan, E. Chai, K. Sundaresan, L. Qiu, M. A. Khojastepour, and S. Rangarajan, "Rio: A pervasive RFID-based touch gesture interface," in *Proc. 23rd Annu. Int. Conf. Mobile Comput. Netw.*, 2017, pp. 261–274.

[23] H. Li, C. Ye, and A. P. Sample, "IDSense: A human object interaction detection system based on passive UHF RFID," in *Proc. 33rd Annu. ACM Conf. Hum. Factors Comput. Syst.*, 2015, pp. 2555–2564.

[24] C. Gao, Y. Li, and X. Zhang, "LiveTag: Sensing human-object interaction through passive chipless WiFi tags," in *Proc. 15th USENIX Symp. Netw. Syst. Design Implement. (NSDI)*, 2018, pp. 533–546.

[25] N. Marquardt, A. S. Taylor, N. Villar, and S. Greenberg, "Rethinking RFID: Awareness and control for interaction with RFID systems," in *Proc. SIGCHI Conf. Hum. Factors Comput. Syst.*, 2010, pp. 2307–2316.

[26] A. P. Sample, D. J. Yeager, and J. R. Smith, "A capacitive touch interface for passive RFID tags," in *Proc. IEEE Int. Conf. RFID*, Apr. 2009, pp. 103–109.

[27] T. M. Simon, B. H. Thomas, R. T. Smith, and M. Smith, "Adding input controls and sensors to RFID tags to support dynamic tangible user interfaces," in *Proc. 8th Int. Conf. Tangible, Embedded Embodied Interact. (TEI)*, 2013, pp. 165–172.

[28] A. Schmidt, H.-W. Gellersen, and C. Merz, "Enabling implicit human computer interaction: A wearable RFID-tag reader," in *Dig. Papers. 4th Int. Symp. Wearable Comput.*, Oct. 2000, pp. 193–194.

[29] H. Li *et al.*, "Paperid: A technique for drawing functional battery-free wireless interfaces on paper," in *Proc. CHI Conf. Hum. Factors Comput. Syst.*, 2016, pp. 5885–5896.

[30] H. Li *et al.*, "A miniature layered SAW contact stress sensor for operation in cramped metallic slits," *Instrum. Exp. Techn.*, vol. 61, no. 4, pp. 610–617, Jul. 2018.

[31] X. Yi, T. Wu, Y. Wang, R. T. Leon, M. M. Tentzeris, and G. Lantz, "Passive wireless smart-skin sensor using RFID-based folded patch antennas," *Int. J. Smart Nano Mater.*, vol. 2, no. 1, pp. 22–38, Feb. 2011.

[32] T. T. Thai, H. Aubert, P. Pons, M. M. Tentzeris, and R. Plana, "Design of a highly sensitive wireless passive RF strain transducer," in *IEEE MTT-S Int. Microw. Symp. Dig.*, Jun. 2011, pp. 1–4.

[33] J. R. Humphries and D. C. Malocha, "Passive, wireless SAW OFC strain sensor," in *Proc. IEEE Int. Freq. Control Symp.*, May 2012, pp. 1–6.

[34] J. Bareisis, "Stiffness and strength of multilayer beams," *J. Composite Mater.*, vol. 40, no. 6, pp. 515–531, Mar. 2006.

[35] R. Hartley. (Dec. 1, 2020). *RF/Microwave PC Board Design and Layout*. [Online]. Available: https://www.jlab.org/accel/eecad/pdf/050rfdesign.pdf

[36] R. C. Johnson, "Design of linear double tapers in rectangular waveguides," *IEEE Trans. Microw. Theory Techn.*, vol. 7, no. 3, pp. 374–378, Jul. 1959.

[37] P. Zhang, C. Josephson, D. Bharadia, and S. Katti, "FreeRider: Backscatter communication using commodity radios," in *Proc. 13th Int. Conf. Emerg. Netw. Exp. Technol.*, New York, NY, USA, Nov. 2017, pp. 389–401, doi: 10.1145/3143361.3143374.

[38] P. Zhang, D. Bharadia, K. Joshi, and S. Katti, "HitchHike: Practical backscatter using commodity WiFi," in *Proc. 14th ACM Conf. Embedded Netw. Sensor Syst. (CD-ROM)*, New York, NY, USA, Nov. 2016, p. 259, doi: 10.1145/2994551.2994565.

[39] Z. Luo, Q. Zhang, Y. Ma, M. Singh, and F. Adib, "3D backscatter localization for fine-grained robotics," in *Proc. 16th USENIX Symp. Netw. Syst. Design Implement. (NSDI)*, 2019, pp. 765–782.

[40] A. Gupta *et al.*, "Wi-chlorian: Wireless sensing and localization of contact forces on a space continuum," 2020, *arXiv:2012.15412*. [Online]. Available: http://arxiv.org/abs/2012.15412

[41] S. K. S. Gupta, S. Lalwani, Y. Prakash, E. Elsharawy, and L. Schwiebert, "Towards a propagation model for wireless biomedical applications," in *Proc. IEEE Int. Conf. Commun. (ICC)*, vol. 3, May 2003, pp. 1993–1997.

[42] D. Vasisht, G. Zhang, O. Abari, H.-M. Lu, J. Flanz, and D. Katabi, "In-body backscatter communication and localization," in *Proc. Conf. ACM Special Interest Group Data Commun.*, Aug. 2018, pp. 132–146.

[43] D. Steck, J. Qu, S. B. Kordmahale, D. Tscharnuter, A. Muliana, and J. Kameoka, "Mechanical responses of ecoflex silicone rubber: Compressible and incompressible behaviors," *J. Appl. Polym. Sci.*, vol. 136, no. 5, p. 47025, Feb. 2019.

[44] P. P. Wang, C. Zhang, H. Yang, D. Bharadia, and P. P. Mercier, "20.1 A 28 μW IoT tag that can communicate with commodity WiFi transceivers via a single-side-band QPSK backscatter communication technique," in *IEEE Int. Solid-State Circuits Conf. (ISSCC) Dig. Tech. Papers*, Feb. 2020, pp. 312–314.

[45] S. Bokhari, "Precision delay matching by trace length control in printed circuit boards," in *Proc. Can. Conf. Electr. Comput. Eng.*, May 2006, pp. 799–802.

Cédric Girerd received the bachelor's degree in mechatronics from SIGMA Clermont, the M.Sc. degree in robotics from the University of Blaise Pascal, Clermont-Ferrand, France, in 2014, and the Ph.D. degree in robotics from the University of Strasbourg, France, in 2018. He is currently working as a Postdoctoral Researcher with the University of California, San Diego. His research focuses on the design and control of continuum robots.

Qiming Zhang is currently pursuing the master's degree in bioengineering with the University of California, San Diego. His research interests include the development of surgical robotics and bio-inspired instruments.

Agrim Gupta received the B.Tech. and M.Tech. (Hons.) degrees from the Indian Institute of Technology Bombay in 2019, with Undergraduate Research Award for his thesis work on MIMO-OFDM precoding. He is currently pursuing the Ph.D. degree with the University of California, San Diego (UCSD) with the WCSNG research group headed by Prof. Dinesh Bharadia. His research focuses on low-power wireless sensing, wireless localization, and MIMO systems.

Manideep Dunna received the B.Tech. and M.Tech. (Hons.) degrees from the Indian Institute of Technology Madras in 2017 and 2018, respectively. He is currently pursuing the Ph.D. degree with the University of California, San Diego (UCSD), with the WCSNG research group. His research focuses on using backscatter techniques for low power wireless relays. He was a recipient of the Charles Lee Powell fellowship at UCSD.

Dinesh Bharadia (Member, IEEE) received the bachelor's degree in electrical engineering from the Indian Institute of Technology, Kanpur, in 2010, and the Ph.D. degree from the Electrical Engineering Department, Stanford University. He is an Assistant Professor with UC San Diego, where he leads the wireless communication sensing and networking group (WCSNG). His research interests include advancing the theory and design of modern wireless communication and sensing systems, and low-power networks.

In recognition of his research, he was named a Marconi Young Scholar for outstanding wireless research and awarded the Michael Dukkakis Leadership award. He was also named as one of the top 35 Innovators under 35 in the world by MIT Technology Review in 2016 and worldwide Forbes 30 under and 30 for Science category in 2018. His Ph.D. thesis invalidated a long-held assumption in wireless communication by building full-duplex radios. From 2013 to 2015, he was a Principal Scientist for Kumu Networks, where he worked to commercialize his research on full-duplex radios, building a product which underwent successful field trials at Tier 1 network providers worldwide like Deutsche Telekom and SK Telecom. He was a recipient of the Stanford Graduate Fellowship, as well as a gold medal at IIT Kanpur for graduating at the top of his class.

Tania. K. Morimoto (Member, IEEE) received the B.S. degree from the Massachusetts Institute of Technology, Cambridge, MA, in 2012, and the M.S. and Ph.D. degrees from Stanford University, Stanford, CA, in 2015 and 2017, respectively, all in mechanical engineering. She is currently an Assistant Professor of Mechanical and Aerospace Engineering and an Assistant Professor of Surgery with the University of California, San Diego. Her research interests include robotics, haptics, and engineering education.